

Highlights

Benchmarking Deep Learning-Based Methods for Irradiance Nowcasting with Sky Images

Lorenzo F. C. Varaschin, Danilo Silva

- Solar irradiance nowcasting using all sky images (ASI).
- Benchmarking deep learning architectures for the irradiance nowcasting task.
- A novel method for sky image and irradiance timestamp alignment is proposed.
- Different model target variables are thoroughly investigated.
- Findings proved consistent across three widely-used solar irradiance datasets.

Benchmarking Deep Learning-Based Methods for Irradiance Nowcasting with Sky Images

Lorenzo F. C. Varaschin¹, Danilo Silva¹

^a*Department of Electrical Engineering, Federal University of Santa Catarina, Florianópolis, Santa Catarina, Brazil*

Abstract

To address the high levels of uncertainty associated with photovoltaic energy, an increasing number of studies focusing on short-term solar forecasting have been published. Most of these studies use deep learning-based models to directly forecast a solar irradiance or photovoltaic power value given an input of sky image sequences. Recently, however, advances in generative modeling have led to approaches that divide the forecasting problem into two sub-problems: 1) future event prediction, i.e. generating future sky images; and 2) solar irradiance or photovoltaic power nowcasting, i.e. predicting the concurrent value from a single image. One such approach is the SkyGPT model, where they show that the potential for improvement is much larger for the nowcasting model than for the generative model. Thus, in this paper, we focus on the solar irradiance nowcasting problem and conduct an extensive benchmark of deep learning architectures across the widely-used Folsom, SIRTa and NREL datasets. Moreover, we perform ablation experiments on different training configurations and data processing techniques, including the choice of the target variable used for training and adjustments of the timestamp alignment between images and irradiance measurements. In particular, we draw attention to a potential error associated with the sky image timestamps in the Folsom dataset and a possible fix is discussed. All our results are reported in terms of both the root mean squared error and the mean absolute error and, by leveraging the three datasets, we demonstrate that our findings are consistent across different solar stations.

Keywords: Solar Irradiance, Nowcasting, Forecasting, Deep Learning, Sky Images, Computer Vision

1. Introduction

Solar photovoltaic (PV) energy, which harvests the Sun's energy directly into electric energy by using semiconductor cells, has seen an exponential growth in recent years [1]. This has brought forth a new set of challenges to the electrical grid operators [2–5], due to the intermittent and uncertain nature of this energy source [6, 7]. The primary cause of uncertainty in PV power generation is the presence of clouds, which can abruptly increase or decrease the amount of solar radiation harnessed by PV panels at any given time. Consequently, a large number of studies have been published in recent years with the goal of creating accurate solar forecasting models.

In the very short term solar forecasting (≤ 60 minutes forecasting horizon), all sky image (ASI) based models have achieved state of the art results, due to their ability to capture the cloud information with a very high spatio-temporal resolution [8]. These images are typically combined with convolutional neural networks (CNN), which extract features from the images that will be used to predict the solar value. The following paragraphs briefly describe some of these approaches.

The authors of [9] use a ResNet18 architecture [10] to encode the image features, which are then used to predict the solar irradiance 5 to 10 minutes ahead. However, instead of feeding a static image to the model, they stack multiple images at different timestamps and gain up to a 7% performance boost. The method proposed in [11] used a 3D CNN [12] to forecast the clear sky index k_t , which results in a 15.2% improvement over the smart persistence model. In [13], a benchmark study of

four different architectures (CNN, CNN+LSTM, 3D-CNN and ConvLSTM) is made and, while the more complex models tend to perform better, it is shown that they all share a fundamental problem: the prediction of future irradiance values often lag behind the ground truth measurements. A multi-modal transformer based framework is proposed in [14], where the solar irradiance time series is encoded by a transformer [15], and the sky images are transformed into optical flow maps and encoded by a vision transformer [16], which are then fused with a cross modality attention block to predict the solar irradiance up to 30 minutes ahead. In [17], a VGG16 [18] inspired model is developed specifically for the solar irradiance forecasting task, the SolarNet model, which outperformed several of their benchmark models. In [19], different input and output configurations are explored for the Sunset model, which is another model specifically designed for the solar forecasting task, but focuses on the solar PV power instead of solar irradiance.

The methodology proposed in [20] is particularly interesting as it separates the future event prediction task from the irradiance mapping task. This is achieved by using a sky image generation model, SkyGPT, which is trained auto-regressively to predict future sky images based on past image sequences. With the generated future sky image, a modified version of the U-Net architecture [21] is then used to predict the concurrent PV power. By decoupling the future event prediction task (SkyGPT) from the PV power nowcasting task (U-Net), they demonstrate that improving the SkyGPT model (such that it could perfectly predict the future sky image) would only boost the performance by 13%, whereas improving the nowcasting model could yield

up to a 64% a performance boost (see Figure 7 of [20]).

Inspired by the larger potential improvement, this study focuses primarily on the solar irradiance nowcasting task, using exclusively sky images as input, i.e. given an image at timestamp t , we want to predict the corresponding irradiance value at the same timestamp t . Although this is different from PV power nowcasting, we expect the results to generalize well across both tasks, since they share the same underlying nature and are highly correlated.

Compared to solar forecasting, fewer studies have tackled the solar nowcasting task. In [22] they perform solar irradiance nowcasting and show that appending a Sun mask as a fourth channel to the images significantly increases the nowcasting performance, which we also investigate in this study. In [23] they adapt the Sunset model for the solar PV power nowcasting task, which is used in this study for the irradiance nowcasting.

We begin our study by conducting an extensive benchmark of ten different deep learning architectures across the Folsom, SARTA and NREL datasets, which are three datasets commonly used in the solar forecasting literature. We then perform several ablation experiments, including the choice of the target variable used for training and adjusting the timestamp alignment between the images and irradiance measurements. All of our experiments are evaluated using the root mean squared error (RMSE) and mean absolute error (MAE) and we show that our findings are consistent across all three datasets. Our main contributions can be summarized as follows:

1. We conduct an extensive benchmark of deep learning architectures across three solar irradiance datasets and find that the ResNet50 architecture provides significant gains over the U-Net architecture used in [20];
2. We demonstrate that appending a Sun mask as a fourth channel to the images as in [22] improves the performance when the model’s target variable is the unnormalized solar irradiance value, but is detrimental otherwise;
3. We demonstrate that the Folsom dataset contains an error associated with their sky image timestamps and a potential fix is investigated;
4. We demonstrate that shifting the irradiance measurements of the training set by a few seconds in time can significantly improve the test set performance.

The rest of this article is structured as follows: [section 2](#) briefly describes the fundamental concepts of solar irradiance, such as the different irradiance components and clear sky models; [section 3](#) describes the three datasets that were used in this study, as well as the different processing steps that were applied; [section 4](#) describes our methods, where we go into detail about our trained models and evaluation metrics; [section 5](#) details all the results and experiments conducted in this study; [section 6](#) concludes the article.

2. Solar Irradiance Fundamentals

2.1. Irradiance Components

Solar irradiance is a measurement of the rate of solar radiation energy that arrives at a surface area and is typically

measured in W/m^2 . The mean solar irradiance at the top of the Earth’s atmosphere, also known as the solar constant [24], is approximately $1366 \text{ W}/\text{m}^2$. After entering the Earth’s atmosphere, the solar radiation will be attenuated by the complex interactions with the atmospheric constituents, resulting in two irradiance components at the ground level: diffuse horizontal irradiance (DHI) and direct normal irradiance (DNI). The DHI measures the amount of solar radiation reflecting on a horizontal plane that was scattered by the atmospheric constituents. The DNI measures the amount of solar radiation that is coming directly from the direction of the Sun beam. The sum of these two components on a horizontal plane results in the global horizontal irradiance (GHI), denoted by [Equation 1](#):

$$\text{GHI} = \text{DNI} \times \cos \theta_z + \text{DHI} \quad (1)$$

where θ_z is the zenith angle. This component is the primary focus of this study.

2.2. Clear Sky Models

Predicting the GHI under clear sky conditions is a well-defined problem, and there are hundreds of different clear sky models available in the literature, with varying but generally excellent performances across many different climates [25, 26]. Clear sky models can also be used to obtain the clear sky index k_t , that normalizes the GHI measurement according to [Equation 2](#):

$$k_t = \frac{I}{I^{\text{clr}}} \quad (2)$$

where I is the GHI measurement and I^{clr} is the clear sky GHI predicted by a clear sky model. In this study, the Simplified Solis Clear Sky Model [27] is used.

Intuitively, I^{clr} would represent the highest possible GHI value and k_t should range between 0 (overcast) to 1 (clear sky). However, k_t can assume values greater than 1, not only because of the imperfections of the clear sky model, but mainly due to a phenomenon called *overirradiance* [28], where the presence of clouds actually increases the GHI through solar beam reflection.

Other than normalization, the k_t index and the clear sky prediction I^{clr} can be used to obtain the smart persistence model, which is a naive model that assumes that the current k_t will stay the same throughout the entire forecasting horizon h , as shown in [Equation 3](#). This model is commonly used as a baseline reference for solar forecasting models.

$$I_{t+h} = k_t \times I_{t+h}^{\text{clr}} \quad (3)$$

Another commonly used index is the clearness index K_t [29], which uses the extraterrestrial irradiance instead to normalize the GHI, as depicted in [Equation 5](#)

$$K_t = \frac{I}{I^{\text{extr}}} \quad (4)$$

where I^{extr} is the extraterrestrial GHI. The main advantage of this index is that I^{extr} is much easier to model than I^{clr} , and can be written as:

$$I^{\text{extr}} = I_0 \times \cos \theta_z \quad (5)$$

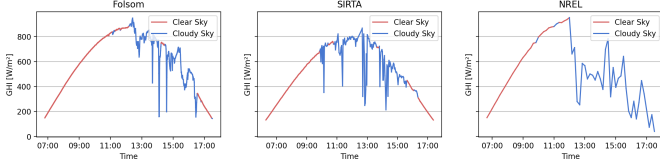


Figure 1: Clear and cloudy sky measurements in each dataset obtained through the Reno algorithm [31].

where I_0 is the solar constant and θ_z is the zenith angle. The choice between both normalization indexes is investigated in [subsubsection 5.2.3](#).

2.3. Detection of Clear Sky Periods

Although sky condition classification is outside the scope of this study, detecting clear/cloudy sky periods can still be used to split the testing set into two smaller subsets, thus providing a more detailed and insightful evaluation of the model’s performance under varying sky conditions. Based on a recent review of 21 different clear sky identification methods [30], and considering the fact that the algorithm is readily available through Python’s `pvlb` library, we chose the Reno [31] method. This is a very simple and effective algorithm that only requires the measured GHI and the expected clear sky GHI data (from the Simplified Solis model, in our case) as inputs. By comparing 5 different statistics of the measured and expected clear sky values over a sliding time window (typically 10 minutes), the algorithm flags a measurement as either clear or cloudy.

Figure 1 shows an example of this method being applied. From our testing, this method works very well for all three datasets in the majority of cases. For more details on this algorithm, we refer the reader to the original paper [31].

3. Data Description and Processing

In this section we describe the raw data used in this study, obtained from three different datasets, as well as the preprocessing pipeline that is made prior to training the models.

3.1. Folsom Dataset

The first dataset used in this study is the Folsom dataset ($\mathcal{D}^{\text{folsom}}$) [32], collected in Folsom, California (38.642° N and 121.148° W), over a 3-year period (2014–2016). This dataset has been widely used by the solar forecasting community [9, 22, 33–38] and it contains a variety of irradiance correlated data, such as sky images, temperature, wind, humidity, among others. In this benchmark study, only the sky images and irradiance data were used.

The sky images were captured during the daylight by a fish-eye lens camera with a resolution of 1536×1536 pixels at a 1-minute sampling interval, totaling over 750,000 images. The GHI and DHI data are collected throughout the entire day by a second generation RSR, which contains two Licor LI-200SZ pyranometers, and the DNI is computed from the measured GHI, DHI and the solar zenith angle θ_z , as per [Equation 1](#). While

all three irradiance data are measured at a 1-second sampling interval, only their 1-minute averages are provided.

Examples of the sky images are shown in the leftmost column of [Figure 2](#) and, unlike the other two datasets, in $\mathcal{D}^{\text{folsom}}$ the camera exposure time is the same for all of the images. The GHI distribution of $\mathcal{D}^{\text{folsom}}$ is shown in the left panel of [Figure 3](#), where it is clear that the density of large irradiance values in this dataset is much higher, i.e. it has a larger number of clear sky instants than the other two datasets.

3.2. SIRTa Dataset

The second dataset we explored was the SIRTa dataset ($\mathcal{D}^{\text{sirta}}$) [39], which was collected in Palaiseau, France (48.713° N and 2.208° E) at the Site Instrumental de Recherche par Télédétection Atmosphérique (SIRTa) observatory. The SIRTa observatory has been rigorously collecting high quality irradiance, sky image and meteorological data for more than 10 years and their dataset is also extensively used by the community [13, 40–45]. For our benchmark study, we only select the 2017–2019 data, as this seems to be the most common choice across the literature.

The sky images were captured with a 768×1024 resolution at a 1-minute sampling interval in 2017 and 2-minute in 2018 and 2019 and come in two forms: 1) a long exposure form that shows the sky in more detail but can have saturated pixels in the area around the Sun; 2) a short exposure form that shows the area around the Sun less saturated and in more detail, but the rest of the sky is shown in less detail (middle images of [Figure 2](#)). The GHI and DHI are measured by a CMP22 pyranometer and the DNI is measured by a CHP1 pyrheliometer, all at a 1-second sampling interval, but only the 1-minute averages are provided.

Compared to the other two datasets, the GHI distribution in $\mathcal{D}^{\text{sirta}}$ (middle panel of [Figure 3](#)) is much more concentrated at lower values, i.e. this dataset has much more cloudy/overcast samples which, generally speaking, are much harder for the models to learn than clear sky samples.

3.3. NREL Dataset

Lastly, we also analyzed the National Renewable Energy Laboratory (NREL) dataset ($\mathcal{D}^{\text{nrel}}$) [46], collected at NREL’s Solar Radiation Research Laboratory (SRRL), located in Golden, Colorado (39.742° N and 105.18° W). The SRRL has been measuring irradiance correlated data since 1981 and, once again, many studies have been published using this dataset: [14, 47–50]. For our benchmark studies, we only selected the sky images and irradiance data collected from 2020 to 2023. It is important to note that $\mathcal{D}^{\text{nrel}}$ provides multiple measurements for the same type of variable, for the sake of redundancy. In our case, the irradiance data used was:

- DNI: measured by the CHP1-1 pyrheliometer;
- DHI: measured by the CM22-1 pyranometer;
- GHI: computed from the two above and the solar zenith angle θ_z as per [Equation 1](#).

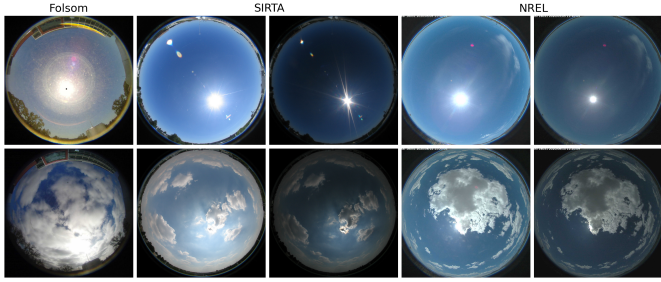


Figure 2: Sky image examples for each dataset used in this study. $\mathcal{D}^{\text{sirta}}$ and $\mathcal{D}^{\text{nrel}}$ also provide a short exposure alternative for each image, so that the area around the Sun can be shown in greater detail. The depicted images were cropped such that they have the same shape.

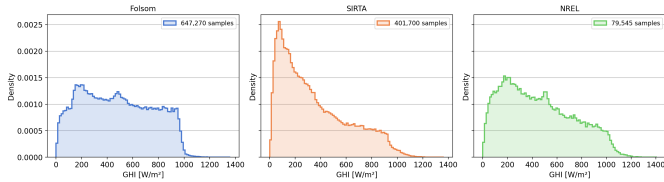


Figure 3: The GHI data distributions for the three datasets used in this study, plotted after the data processing pipeline.

Like in the previous two datasets, the irradiance data in $\mathcal{D}^{\text{nrel}}$ are 1-minute averages and their GHI distribution is plotted in the right panel of Figure 3.

The sky images are provided at a 1536×1536 pixel resolution in both long and short exposures (rightmost images of Figure 2), however they are only available once every 10 minutes, which makes this a much smaller dataset compared to the other two (for our selected years in each dataset). The impact that a smaller training dataset has on the model performance is further discussed in subsection 5.2.5

3.4. Sky Image Data Processing

The image processing was essentially the same for all 3 datasets. First we compute the mean image of each dataset (using only the long exposure images for $\mathcal{D}^{\text{sirta}}$ and $\mathcal{D}^{\text{nrel}}$) and then define a circular region of interest (ROI), with radius R and center C , which is used as a binary mask for that dataset. These masks are applied to all the images in their respective datasets to cancel every pixel outside their ROI. Following this, we center crop the images on C with length $2R$. Finally, the images are downsampled to a 64×64 resolution using the Python’s PIL library. To avoid any potential JPEG compression losses [51], the resized images are saved to disk in .npy format.

3.5. Irradiance Data Processing

The irradiance data processing was also largely the same for all 3 datasets. First, we resample the data to a 1-second frequency through linear interpolation (more details on why this is done in the following section). To avoid large interpolation errors, this is only done for the samples that are 1-minute apart, i.e. periods with 2 or more minutes of missing data are discarded. Following the linear interpolation, we remove all samples where

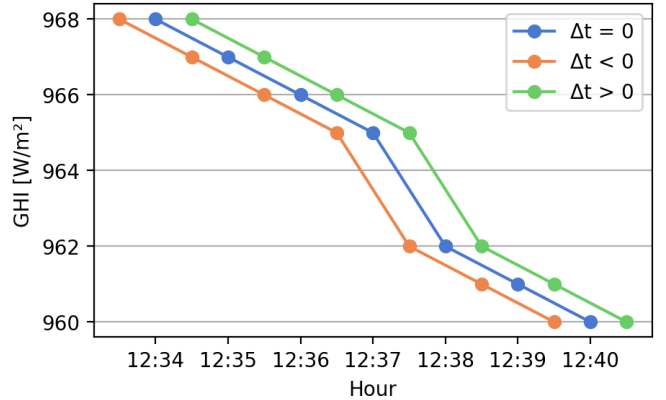


Figure 4: The effect of applying a Δt to the irradiance time series. A negative Δt essentially advances the samples in time, by shifting the curve to the left, whereas a positive Δt has the opposite effect, by shifting it to the right.

$\theta_z > 80^\circ$, as these samples provide little information and the GHI is always low.

The next processing step is **only applied to the training set** of each dataset (see subsection 3.8 for the train/test splits) and consists of shifting the irradiance measurements in time by applying a time offset (Δt), which we do according to (6)

$$T_{\text{new}} = T_{\text{orig.}} + \Delta t \quad (6)$$

where T_{new} and $T_{\text{orig.}}$ are the new and original irradiance measurement timestamps, respectively. If a $\Delta t < 0$ is applied, then we are advancing the irradiance series in time, relative to the sky image series, whereas a $\Delta t > 0$ would have the opposite effect, as shown in Figure 4. Depending on how these irradiance values were averaged, we hypothesize that this can be beneficial. For instance, if the value of I at 14:00:00 represents the average GHI values from 13:59:01 to 14:00:00 (backward average), then a $\Delta t < 0$ could diminish the delay introduced by such an average. However, applying a Δt to the testing set would result in different labels for every searched Δt , possibly leading to an unfair evaluation. Thus, we only shift the irradiance measurements in the training set, by -20s, 10s and -20s in $\mathcal{D}^{\text{folsom}}$, $\mathcal{D}^{\text{sirta}}$ and $\mathcal{D}^{\text{nrel}}$, respectively. Other time offsets are investigated in subsection 5.2.2.

3.6. Sky Image and Irradiance Alignment

Our sky image and irradiance alignment for each dataset was very different, especially for $\mathcal{D}^{\text{folsom}}$. Initially, we aligned the sky images with the irradiance data based on the name of the image files, i.e. an image sample x_t^{folsom} , with file name timestamp t , was labeled with the irradiance sample I_t^{folsom} . While this seems like the most natural choice, we noticed some strange behavior when, for example, two images captured only minutes apart were labeled with vastly different GHI values, but the image with the Sun exposed was the one with the lower value and the image without the Sun exposed had the higher value. To the best of our knowledge, this unexpected behavior in $\mathcal{D}^{\text{folsom}}$ has not yet been discussed in the literature and, after some extensive error analysis, we found that it is due to a mismatch between

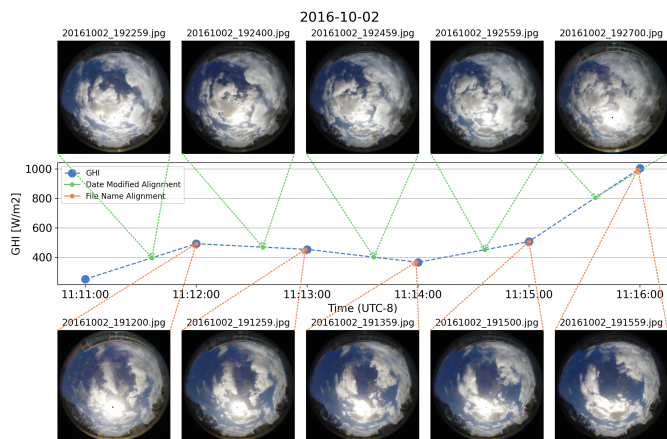


Figure 5: A 5-minute GHI window in $\mathcal{D}^{\text{folsom}}$ showing the corresponding date modified aligned images in the top row and the file name aligned images in the bottom row. The middle row shows the linearly interpolated GHI data, plotted in UTC-8 timezone for better visualization, while the original file names (titles above each image) are in UTC+0 timezone.

the image file names and their corresponding date modified metadata, with the latter seeming to be the correct timestamp. In Figure 5 we show a 5 minute GHI window in the middle row, with the image **date modified** alignment in the top row and the image **file name** alignment in the bottom row. It shows that the GHI began at a medium to low value, before jumping to 1000 W/m^2 at 11:16:00. This massive increase indicates that the Sun must have been uncovered during this period, which does indeed happen with the date modified alignment. However, with the file name alignment, the opposite happens, the Sun is uncovered at 11:12:00, when the GHI is at a medium value, but is covered at 11:16:00, when the GHI is at a high value, which is very counterintuitive.

In the 5-minute window being shown in Figure 5, the file name is approximately 11:30 minutes ahead of the date modified, but, from our analysis, we found that this difference is shifting throughout the dataset, which can be seen in Figure 6, that shows the daily average difference between the file name timestamp and the date modified timestamp. A positive value means that the file name is ahead of the date modified and vice-versa. As time passes, this difference seem to be shifting towards 0 seconds, which would be ideal, however 3 major jumps occur in Jun-2014, Feb-2015 and Sep-2016, which significantly aggravate the problem, especially towards the end of 2016, where a 12-minute difference can be observed between the two. This means that, assuming the date modified is the correct timestamps of the images (Figure 5 indicates that this is a fair assumption), then aligning the irradiance data with the images based on their file names would always result in incorrect labels for the model to learn, as well as for model evaluation. Therefore, we use the date modified alignment in $\mathcal{D}^{\text{folsom}}$, except during the experiment in subsection 5.2.1, where we provide a more quantitative analysis on this issue.

As a precautionary measure, we also compared the metadata of x^{sirta} and x^{nrel} to their file names, but no inconsistency was found. Therefore, the sky image and irradiance alignment in

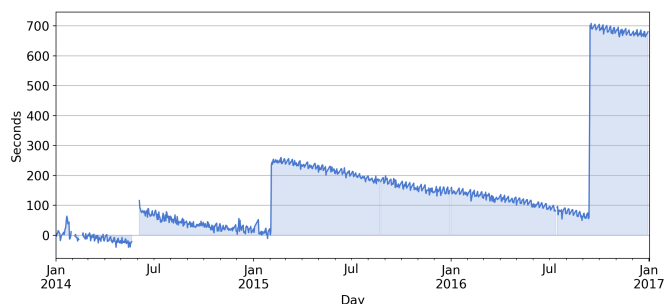


Figure 6: Daily average difference between the file name and date modified of the image data in $\mathcal{D}^{\text{folsom}}$. A positive value indicates that the file name is ahead of the date modified and vice-versa.

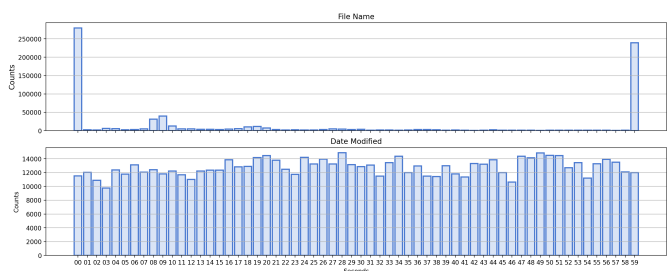


Figure 7: Image timestamp second counts in $\mathcal{D}^{\text{folsom}}$. The upper axis shows that the file name timestamps are mostly synchronized at either :00 or :59 seconds (i.e. the file ends in “00.jpg” or “59.jpg”). On the other hand, the lower axis shows that the date modified timestamps are uniformly spaced throughout the 60 possible values.

those two datasets was done based on the image file names, as that is the most natural choice.

Another thing to keep in mind when aligning the images with the irradiance data is the irregularity in the image timestamps, which is especially true assuming the date modified as the correct timestamp (see Figure 7). Since the irradiance samples are all synchronized at :00 seconds, aligning an image that was captured at :30 seconds with the nearest irradiance sample could result in a large error, especially in fast moving cloud conditions. To mitigate this problem, we linearly interpolate the irradiance samples before the alignment. While this mostly affects $\mathcal{D}^{\text{folsom}}$, the linear interpolation is applied to the other two datasets as well.

3.7. Sun Mask Generation

In subsection 5.2.6 we conduct an ablation experiment where we use a Sun mask as an additional input to the now-casting model, which has shown to significantly benefit the performance in [22]. First, we compute the distance of the Sun center from the center of the image plane, denoted by R , which is a function of the focal length of the camera f and the angle from the optical axis Φ . This mapping function will vary, since different types of lenses will have different projection types [52]. For the stereographic projection, the mapping function is $R = 2f \tan \frac{\Phi}{2}$, and for the equidistant projection the mapping function is $R = f\Phi$, where Φ is replaced by the zenith angle θ_z . Following this, we compute the Sun center coordinates on the

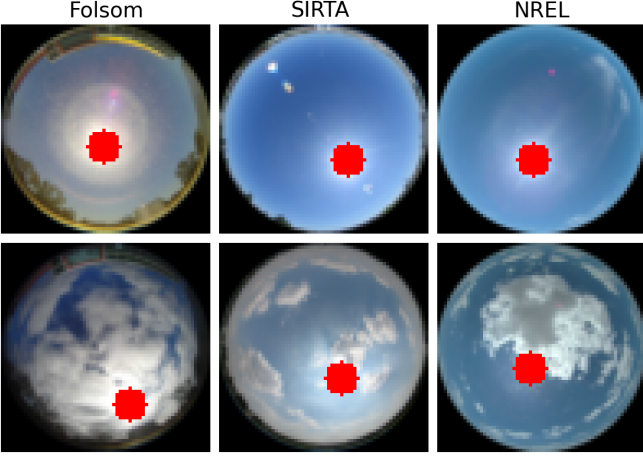


Figure 8: Sun mask examples applied to the 64×64 images in all three datasets under cloudy and clear sky conditions. For a 64×64 image, the circle has a 5 pixel radius and is centered on x_p and y_p .

Table 1: Sun center localization parameters for each dataset. f is the focal length and θ_c is the correction angle.

Dataset	Projection	f	θ_c
Folsom	Stereographic	0.48	165°
SIRTA	Equidistant	0.63	182°
NREL	Equidistant	0.67	180°

image plane according to Equation 7 and Equation 8.

$$x_c = R \sin(\theta_a - \theta_c) \quad (7)$$

$$y_c = R \cos(\theta_a - \theta_c) \quad (8)$$

where θ_a is the azimuth angle and θ_c is a correction angle that compensates for the orientation of the camera. To transform x_c and y_c to pixel coordinates and obtain x_p and y_p , we apply:

$$x_p = \frac{W}{2}(1 + x_c) \quad (9)$$

$$y_p = \frac{W}{2}(1 + y_c) \quad (10)$$

where W is the image width. Finally, we create the binary Sun mask as a circle with a 5 pixel radius (for $W = 64$) and centered on x_p and y_p , as shown in Figure 8.

In the original paper, they only apply this mask in $\mathcal{D}^{\text{folsom}}$, in which they determine the stereographic projection for the R mapping function, $f = 0.48$ and $\theta_c = 165^\circ$. However, using these same parameters in $\mathcal{D}^{\text{sirta}}$ and $\mathcal{D}^{\text{nrel}}$ yielded bad results, so, through trial and error, we tuned them according to Table 1. The other two parameters, θ_z and θ_a , are obtained with Python’s pvlib library. For more details on this algorithm, we refer the reader to the original paper [22].

3.8. Train, Test and Validation Splits

All three datasets are first split into a train set, which is used to optimize the parameters of the models, and a testing set,

Table 2: Number of samples for each set after the application of all the pre-processing steps.

Dataset	Train	Test		
		All	Clear	Cloudy
Folsom	426,515	220,755	117,423	103,332
SIRTA	297,774	103,926	18,447	85,479
NREL	59,444	20,101	7,300	12,801

which is used to evaluate said models. To account for all possible seasonal variations, we select one full year for testing, which was 2016, 2019 and 2023 for $\mathcal{D}^{\text{folsom}}$, $\mathcal{D}^{\text{sirta}}$ and $\mathcal{D}^{\text{nrel}}$, respectively. Moreover, the algorithm described in subsection 2.3 is used to further split the testing set into two additional sets: a clear sky and a cloudy sky set.

The remaining years of each data set are used for the train set. In order to optimize the hyperparameters of the model, we split the full train set into a smaller train set and a validation set using K -Fold cross validation (CV). More specifically, we use stratified group K -Fold (with $K = 5$), where each day is assigned to a different group (to avoid leaking samples from the same day in the training/validation sets) and each bin in the original train set (see Figure 3) is assigned to a different class to maintain the original irradiance distribution in all 5 folds. After optimizing the hyperparameters of each model, we use the full train set to train a final model, which will be evaluated on the test set. Table 2 shows the number of samples in each set, after the application of all the pre-processing steps.

4. Methods

In this section we go into detail about our training setup, the model architectures we trained and our evaluation metrics. As the main objective of this study is to benchmark different model architectures for the on-site irradiance nowcasting task, all of our models are trained and evaluated separately for each dataset, however we also evaluate the aggregated performance across all three datasets.

4.1. Training Setup

Given an input image x_i , each model produces an estimate \hat{I}_i of the concurrent GHI measurement I_i . As described in subsection 3.6, the sky image and irradiance measurement pairs $\{x_i, I_i\}$ are created using the image file name timestamps in $\mathcal{D}^{\text{sirta}}$ and $\mathcal{D}^{\text{nrel}}$ and the image date modified timestamps in $\mathcal{D}^{\text{folsom}}$. The models are trained to minimize the Mean Squared Error (MSE) loss function given by

$$L_{\text{MSE}} = \frac{1}{B} \sum_{i=1}^B (y_i - \hat{y}_i)^2 \quad (11)$$

where B is the batch size, y_i is the ground truth label of the i^{th} sample and \hat{y}_i is the model’s output for the i^{th} sample. Following previous work [11, 42], we use the clear sky index as our default

target variable, $y_i = k_{t,i}$, which implies that the GHI estimate is computed as $\hat{I}_i = I^{\text{clr}} \hat{k}_{t,i}$, where $\hat{k}_{t,i} = \hat{y}_i$. Other target variables and loss functions are explored in [subsection 5.2.3](#).

Our models are trained with a learning rate that exponentially decays from its initial value lr_0 to $\frac{\text{lr}_0}{10}$ during the first 75% of training according to [Equation 12](#)

$$\text{lr}_i = \text{lr}_{i-1} \times e^{\frac{\ln 1/10}{0.75 \times n_{\text{epochs}}}} \quad (12)$$

where n_{epochs} is the total number of epochs and $0 < i < 0.75 \times n_{\text{epochs}}$. The remaining 25% of training is done with the learning rate fixed at $\frac{\text{lr}_0}{10}$ and we start averaging the weights of the model at the end of every epoch, as this has shown to lead to better generalization [53]. Each model is trained on a NVIDIA GeForce RTX 3090 GPU (24 GB memory) for a total of 16 epochs, except during hyperparameter optimization, where they are only trained for 8 epochs to save on computational time. Details on the initial learning rate and other hyperparameters values are described in the following section.

4.2. Model Architectures and Hyperparameter Optimization

We train and compare 10 different model architectures in this study, 7 of which are popular deep learning architectures used in many computer vision tasks and 3 that were designed/adapted specifically for the solar task. The first 7 include: ResNets (18, 34 and 50) [10]; VGG16 [18]; EfficientNetV2-S [54]; RegNetY-1.6GF [55]; MobileNetV2 [56]. We use the Pytorch implementation of these models and always initialize them with their pre-trained weights, except for the final layer, since we change it to only predict a single output, corresponding to the irradiance value. The other 3 models already output a single value, since they were designed for the solar task, however they are randomly initialized since we were unable to access their pre-trained weights. They are: SolarNet [17]; Sunset [19, 23]; and a modified version of the popular U-Net [21] architecture, modified in [20].

We search 30 different hyperparameter combinations per model per dataset, totaling 900 different searches, which are made through Bayesian optimization [57] using the train/validation splits defined in [subsection 3.8](#) and with the goal of minimizing the average validation loss across all 5 folds. For hyperparameter optimization, we reduce the number of training epochs to 8 and only use 10% of the training data in each dataset. The hyperparameter search space is shown in [Table 3](#).

4.3. Evaluation Metrics

A large variety of metrics have been proposed by the solar forecasting community in order to assess the quality of a model’s predictions in the most insightful way possible [60–62]. In this study, we only evaluate the root mean squared error (RMSE) and the mean absolute error (MAE), which are well established metrics for evaluating the overall fit of the predictions:

$$\text{RMSE} = \sqrt{\frac{1}{N} \sum_{i=1}^N (I_i - \hat{I}_i)^2} \quad (13)$$

Table 3: Hyperparameter search space for all the models and datasets. The PyTorch weight initialization is made for all the layers up to the last in the 7 models already implemented in PyTorch. The other 3 models are always randomly initialized with a fixed seed.

Hyperparameter	Searched Values
Initial Learning Rate (lr_0)	$[1, 2, 3, 4, 5, 6, 7, 8, 9, 10] \times 10^{-4}$
Weight Initialization (θ_0)	PyTorch, Random
Weight Decay (λ)	Uniform(0, 10^{-3})
Batch Size (B)	64, 128
Optimizer (Op.)	SGD, Adam [58], AdamW [59]
Dropout (p)	0.0, 0.1, 0.2, 0.3, 0.4, 0.5, 0.6, 0.7

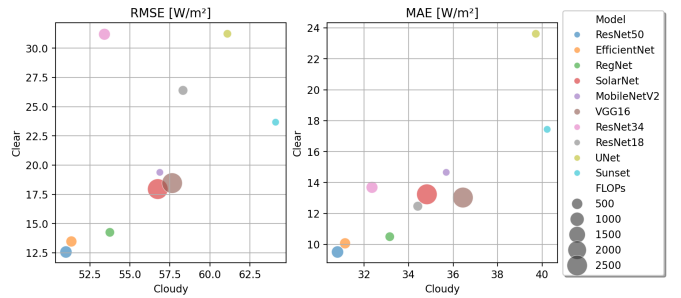


Figure 9: Cloudy and clear sky scatter plot showing the aggregated performance of all ten models. The left panel shows the RMSE performance and the right panel shows the MAE. Marker sizes are scaled according to the number of FLOPs for each model.

$$\text{MAE} = \frac{1}{N} \sum_{i=1}^N |I_i - \hat{I}_i| \quad (14)$$

where N is the number of samples, I_i is the ground truth measurement of the GHI for the i^{th} sample and \hat{I}_i is the model’s estimate of the GHI for the i^{th} sample. We employ the RMSE as our main ranking metric, since it penalizes larger errors more heavily than the MAE. Note that, regardless of our choice for the model’s target variable, the evaluation metrics are always expressed in terms of the GHI (W/m^2), as that is the variable of interest.

5. Experiments and Results

5.1. Model Architectures

[Table 4](#) shows the RMSE and MAE for the test set for all ten models and all three datasets, as well as the aggregated performance across all datasets. From these results, it is clear that the ResNet50 architecture outperforms the others by a healthy margin, especially in comparison to the Sunset and U-Net architectures. The only 2 cases where the ResNet50 was not the best performing architecture was in cloudy sky conditions in $\mathcal{D}^{\text{folsom}}$ (where the EfficientNetV2-S performed better) and in clear sky conditions in $\mathcal{D}^{\text{nrel}}$ (where the VGG16 performed better).

[Figure 9](#) summarizes the aggregated results in [Table 4](#) for both the clear and cloudy sky test subsets.

Table 4: Model architecture benchmark results for all three datasets. The best performing architecture is highlighted in green. The Aggr. dataset refers to the aggregated predictions/ground truth for all three datasets.

Dataset	Sky cond.	RMSE [W/m ²]			MAE [W/m ²]		
		All	Cloudy	Clear	All	Cloudy	Clear
Folsom	EfficientNet	37.39 ± 0.12	52.60 ± 0.18	13.86 ± 0.51	20.87 ± 0.25	32.75 ± 0.20	10.40 ± 0.32
	MobileNetV2	45.17 ± 2.04	62.22 ± 2.11	20.60 ± 3.06	27.94 ± 1.93	41.67 ± 1.87	15.85 ± 2.20
	RegNet	37.68 ± 0.36	53.21 ± 0.37	13.31 ± 0.79	20.91 ± 0.47	33.21 ± 0.39	10.09 ± 0.58
	ResNet18	40.26 ± 0.81	56.31 ± 1.17	16.02 ± 0.57	22.92 ± 0.50	35.18 ± 0.84	12.13 ± 0.37
	ResNet34	45.91 ± 11.74	54.34 ± 0.52	31.65 ± 24.91	22.84 ± 1.84	33.37 ± 0.17	13.57 ± 3.41
	ResNet50	37.21 ± 0.26	52.62 ± 0.35	12.89 ± 0.39	20.58 ± 0.15	32.82 ± 0.25	9.80 ± 0.23
	SolarNet	43.25 ± 1.81	59.87 ± 1.70	18.90 ± 2.93	25.32 ± 1.43	38.12 ± 1.13	14.06 ± 1.69
	Sunset	48.08 ± 2.31	65.34 ± 2.64	24.06 ± 3.70	29.16 ± 2.18	41.89 ± 1.92	17.96 ± 2.85
	UNet	50.12 ± 2.27	64.29 ± 1.45	32.67 ± 5.14	33.57 ± 2.89	43.10 ± 1.47	25.18 ± 4.38
	VGG16	39.64 ± 0.52	55.35 ± 0.57	16.03 ± 0.78	22.91 ± 0.47	35.28 ± 0.46	12.02 ± 0.54
SIRTA	EfficientNet	40.19 ± 0.23	44.00 ± 0.27	11.42 ± 0.42	23.72 ± 0.21	27.00 ± 0.31	8.53 ± 0.43
	MobileNetV2	40.61 ± 0.27	44.44 ± 0.32	11.91 ± 1.00	23.56 ± 0.21	26.72 ± 0.22	8.94 ± 0.67
	RegNet	45.25 ± 2.09	49.03 ± 1.88	19.29 ± 5.48	27.99 ± 1.70	31.05 ± 1.27	13.78 ± 3.74
	ResNet18	44.80 ± 2.24	48.66 ± 2.41	18.21 ± 2.08	27.90 ± 1.74	31.14 ± 1.94	12.89 ± 1.22
	ResNet34	43.72 ± 2.00	46.60 ± 1.22	25.32 ± 9.00	26.71 ± 1.47	28.95 ± 0.91	16.31 ± 4.28
	ResNet50	39.68 ± 0.21	43.46 ± 0.22	10.75 ± 0.56	23.06 ± 0.16	26.30 ± 0.14	8.07 ± 0.42
	SolarNet	42.99 ± 0.58	47.04 ± 0.63	12.57 ± 0.44	25.21 ± 0.43	28.64 ± 0.47	9.31 ± 0.37
	Sunset	46.90 ± 1.03	50.97 ± 0.94	18.77 ± 2.81	29.46 ± 0.96	32.81 ± 0.80	13.94 ± 1.96
	UNet	47.75 ± 1.44	51.31 ± 1.50	25.36 ± 1.72	30.68 ± 0.96	33.33 ± 0.92	18.43 ± 1.29
	VGG16	52.57 ± 2.81	56.16 ± 2.50	30.62 ± 5.96	33.67 ± 2.30	36.30 ± 1.74	21.48 ± 4.92
NREL	EfficientNet	63.40 ± 0.53	78.95 ± 0.60	11.63 ± 1.05	32.22 ± 0.50	45.71 ± 0.29	8.58 ± 0.97
	MobileNetV2	64.81 ± 0.34	80.58 ± 0.45	13.43 ± 1.32	33.73 ± 0.53	47.35 ± 0.35	9.85 ± 1.19
	RegNet	65.06 ± 0.59	81.03 ± 0.72	12.00 ± 0.67	32.94 ± 0.38	46.63 ± 0.21	8.93 ± 0.74
	ResNet18	102.68 ± 45.09	104.77 ± 42.09	79.30 ± 77.36	37.91 ± 5.03	49.94 ± 5.55	16.81 ± 8.69
	ResNet34	65.28 ± 0.99	81.08 ± 1.23	13.90 ± 3.37	33.09 ± 0.35	46.85 ± 0.57	8.96 ± 0.35
	ResNet50	62.10 ± 0.37	77.31 ± 0.50	11.63 ± 0.82	31.47 ± 0.32	44.54 ± 0.34	8.54 ± 0.72
	SolarNet	67.22 ± 0.80	83.67 ± 1.01	12.88 ± 0.45	35.05 ± 0.53	49.37 ± 0.77	9.93 ± 0.41
	Sunset	92.07 ± 2.15	113.58 ± 2.68	26.81 ± 1.42	55.14 ± 1.13	76.44 ± 1.59	17.79 ± 1.03
	UNet	71.34 ± 2.76	88.50 ± 3.43	16.58 ± 1.88	39.38 ± 1.91	55.15 ± 2.74	11.73 ± 1.13
	VGG16	64.68 ± 0.44	80.64 ± 0.55	10.81 ± 0.15	32.69 ± 0.30	46.86 ± 0.44	7.86 ± 0.08
Aggr.	EfficientNet	40.20 ± 0.06	51.33 ± 0.09	13.47 ± 0.44	22.39 ± 0.16	31.14 ± 0.14	10.07 ± 0.29
	MobileNetV2	45.27 ± 1.34	56.87 ± 1.23	19.38 ± 2.74	26.96 ± 1.28	35.69 ± 1.01	14.66 ± 1.89
	RegNet	42.11 ± 0.82	53.74 ± 0.85	14.25 ± 1.37	23.74 ± 0.71	33.15 ± 0.68	10.50 ± 0.79
	ResNet18	48.35 ± 6.32	58.32 ± 6.39	26.39 ± 13.53	25.30 ± 0.72	34.41 ± 1.02	12.47 ± 0.53
	ResNet34	46.96 ± 7.61	53.40 ± 0.33	31.19 ± 21.47	24.60 ± 1.18	32.35 ± 0.30	13.69 ± 2.88
	ResNet50	39.82 ± 0.21	50.99 ± 0.24	12.57 ± 0.36	21.96 ± 0.15	30.80 ± 0.18	9.51 ± 0.22
	SolarNet	44.93 ± 1.29	56.74 ± 1.14	17.95 ± 2.57	25.86 ± 1.03	34.82 ± 0.77	13.24 ± 1.42
	Sunset	51.38 ± 1.20	64.12 ± 1.28	23.67 ± 2.99	30.77 ± 1.20	40.23 ± 0.83	17.44 ± 2.27
	UNet	50.94 ± 1.39	61.10 ± 1.01	31.23 ± 4.38	33.04 ± 1.78	39.72 ± 0.85	23.62 ± 3.55
	VGG16	45.66 ± 0.97	57.64 ± 0.99	18.46 ± 1.41	26.72 ± 0.74	36.44 ± 0.73	13.03 ± 0.76

5.2. Ablation Experiments

Based on the results from the previous section, we then perform several ablation experiments using the ResNet50 model with the goal of investigating the impact that different configurations of pre-processing steps and training setups have on the performance. These configurations are summarized in Table 5. Note that, for the “ Δt ” and “Sample Interval” configuration, the searched values **are only applied to the training set**, while the default values are used for the test set.

5.2.1. Image Timestamps in $\mathcal{D}^{\text{folsom}}$

As mentioned in subsection 3.6, aligning the sky images with the irradiance data in $\mathcal{D}^{\text{folsom}}$ using the image file names led to large label errors and the date modified of the images seemed to be more aligned with the irradiance data timestamps. To the best of our knowledge, this has not yet been reported in the literature so, in order to ascertain that the date modified is truly the correct timestamp for labeling the images in $\mathcal{D}^{\text{folsom}}$, a more quantitative analysis is also needed. To this end, we train two different models, one trained on a file name aligned training set and another on a date modified aligned training set. Both of these models are then evaluated on file named aligned testing set and a date modified aligned testing set, totaling four different train/test image timestamp alignment combinations. All other configurations are kept at their default values, depicted in Table 5.

As shown in Table 6, when both the training set and the testing set are aligned with the date modified timestamp the RMSE drops significantly, confirming the assumptions made in subsection 3.6. Perhaps unsurprisingly, this drop was much larger for the cloudy subset than the clear subset, since, for the majority of clear sky samples, a few minutes difference in alignment results in small GHI differences. On the other hand, under cloudy sky conditions, the sky image and irradiance alignment is much more critical.

Moreover, Table 6 also highlights the fact that evaluating with the date modified alignment is always better than with the file name alignment, even when training with the file name. The reason for this can be attributed to Figure 6, which shows that the file name alignment is much worse in 2016 than in 2014/2015. Since we selected 2014/2015 for training and 2016 for testing, this means that the model can still learn somewhat useful features if trained with the file name alignment. However, evaluation on the file name aligned test set will always result in very large errors, since the alignment is worst in 2016.

5.2.2. Time Shifting Operation

As described in subsection 3.5, we shift the irradiance measurements of the training set by applying a timestamp offset of Δt . For each dataset, we optimize $\Delta t \in \{-30s : 10s : 30s\}$ by applying a 5-fold CV (as described in subsection 4.1) and minimizing the validation loss. We then apply the optimal Δt to the full training set to train the model and evaluate the results on the testing set.

The CV results are depicted in Figure 10, which shows the mean validation set RMSE across all 5 folds, for each dataset. Interestingly, in $\mathcal{D}^{\text{folsom}}$ and $\mathcal{D}^{\text{nrel}}$, the validation RMSE decreases

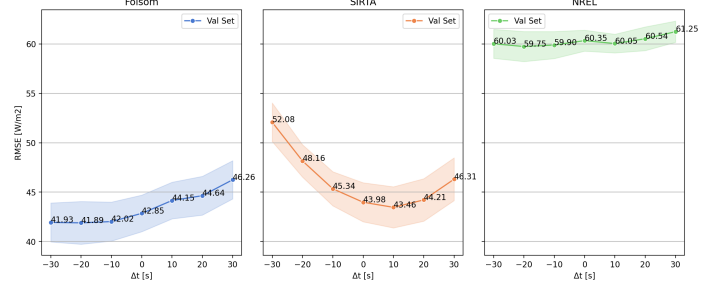


Figure 10: Validation set results for $\mathcal{D}^{\text{folsom}}$, $\mathcal{D}^{\text{sirta}}$ and $\mathcal{D}^{\text{nrel}}$. For each Δt , we report the mean RMSE across all 5 folds, as well as the standard deviation.

slightly for a negative Δt and increases for a positive Δt , but in $\mathcal{D}^{\text{sirta}}$ the opposite happens. This suggests that the type of average applied to the GHI samples in $\mathcal{D}^{\text{folsom}}$ was the same as in $\mathcal{D}^{\text{nrel}}$, but different in $\mathcal{D}^{\text{sirta}}$. The optimal Δt was -20s, 10s and -20s for $\mathcal{D}^{\text{folsom}}$, $\mathcal{D}^{\text{sirta}}$ and $\mathcal{D}^{\text{nrel}}$, respectively.

Regarding the results of the test set, Table 7 shows that using the optimal Δt to train the models always leads to a consistent gain in performance for all datasets, especially in cloudy sky conditions, since the sky image and irradiance alignment is more critical during these periods.

5.2.3. Target Variable and Loss Function

In this experiment, we consider five combinations of target variables and loss functions. Specifically, for the MSE loss (11), we consider three choices for the target variable $y \in \{I, k_t, K_t\}$, resulting in the following expressions for the GHI estimate

$$\hat{I}_i = \begin{cases} \hat{y}_i, & \text{if } y_i = I_i, \\ I^{\text{clr}} \hat{k}_{t,i}, \text{ where } \hat{k}_{t,i} = \hat{y}_i, & \text{if } y_i = k_{t,i}, \\ I^{\text{extr}} \hat{K}_{t,i}, \text{ where } \hat{K}_{t,i} = \hat{y}_i, & \text{if } y_i = K_{t,i}. \end{cases} \quad (15)$$

Although using the raw GHI value as target is the most natural and simple choice, it suffers from the fact that the GHI values will have different scales across different weather seasons. The left panel of Figure 11 depicts a ΔGHI of almost 500 W/m² between the peak GHI value in summer and in winter, which, from their corresponding images, can be inferred based on the distance from the Sun center to the image center. This means that models trained to predict raw GHI values need to encode the Sun’s position in the image with extreme precision in order to be able to generalize its predictions, which can be a difficult task in cloudy sky conditions. By comparison, the k_t value does not show this limitation (right panel of Figure 11), since the seasonal variance of the GHI values is already taken into account by the clear sky model. Another value that is not affected by this seasonal variance is the clearness index K_t , which just normalizes the GHI values by I^{extr} instead of I^{clr} .

While the use of k_t or K_t as target solves the seasonal variance problem, it fails to take into account the diurnal variance of the GHI, i.e. a sample at the end of the day (with low GHI magnitude) will be weighted the same as a sample in the middle of the day (with high GHI magnitude). This is undesirable, since the middle of the day is the period with the higher load, hence

Table 5: Configuration table for all the ablation experiments in this study. The values for a certain configuration are only searched in their respective sections, otherwise the default value is used.

Configuration	Dataset	Searched Values	Default Values
Image Timestamps (5.2.1)	Folsom	File Name, Date Modified	Date Modified
	SIRTA	-	File Name
	NREL	-	File Name
Time off-set Δt (5.2.2)	Folsom	-30s:10s:30s	-20s
	SIRTA	-30s:10s:30s	10s
	NREL	-30s:10s:30s	-20s
Model Target (5.2.3)	Folsom		
	SIRTA	GHI, k_t , K_t , k_t^{weighted} , K_t^{weighted}	k_t
	NREL		
Camera Exposure (5.2.4)	Folsom	Long	
	SIRTA	Short, Long	Long
	NREL	Short, Long	
Sample Interval (5.2.5)	Folsom	1 - 10 min	1 min
	SIRTA	1/2 - 10 min	1/2 min
	NREL	10 min	10 min
Sun Mask (5.2.6)	Folsom		
	SIRTA	Mask, No Mask	No Mask
	NREL		

Table 6: Image timestamp alignment results for the four possible train/test combinations and the different test subsets in $\mathcal{D}^{\text{folsom}}$.

Sky Cond.	Train	Test	RMSE [W/m^2]
All	File Name	File Name	62.52 ± 0.18
	File Name	Date Modif.	56.72 ± 0.13
	Date Modif.	File Name	59.37 ± 0.34
	Date Modif.	Date Modif.	37.21 ± 0.28
Cloudy	File Name	File Name	89.76 ± 0.35
	File Name	Date Modif.	81.19 ± 0.18
	Date Modif.	File Name	85.34 ± 0.48
	Date Modif.	Date Modif.	52.62 ± 0.39
Clear	File Name	File Name	16.05 ± 0.60
	File Name	Date Modif.	15.76 ± 0.57
	Date Modif.	File Name	14.69 ± 0.43
	Date Modif.	Date Modif.	12.89 ± 0.43

Table 7: Test set performance comparison between a 0 second Δt (baseline) and the best performing one, obtained during CV.

Dataset	Δt	RMSE [W/m^2]		
		All	Clear	Cloudy
Folsom	0s	40.24 ± 0.94	15.60 ± 1.36	56.41 ± 1.06
	-20s	37.21 ± 0.26	12.89 ± 0.39	52.62 ± 0.35
SIRTA	0s	41.22 ± 0.54	11.17 ± 0.44	45.15 ± 0.59
	10s	39.68 ± 0.21	10.75 ± 0.56	43.46 ± 0.22
NREL	0s	64.56 ± 0.72	10.71 ± 0.09	80.50 ± 0.91
	-20s	62.10 ± 0.37	11.63 ± 0.82	77.31 ± 0.50

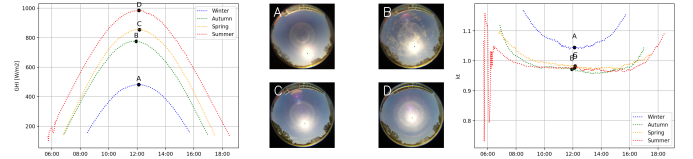


Figure 11: GHI and k_t values comparison for a clear sky day showing the seasonal variance in $\mathcal{D}^{\text{folsom}}$. The left panel shows the GHI values and the right panel shows the k_t values. The corresponding images to each labeled marker are shown in the middle panel.

samples during this period should be weighted more heavily. To solve this, we rescale the model prediction back into the GHI estimate before computing the squared error, leading to the loss function

$$L_{\text{MSE}}^{\text{weighted}} = \frac{1}{B} \sum_{i=1}^B (I^{\text{clr/extr}}(y_i - \hat{y}_i))^2 = \frac{1}{B} \sum_{i=1}^B (I_i - \hat{I}_i)^2 \quad (16)$$

where

$$I^{\text{clr/extr}} = \begin{cases} I^{\text{clr}}, & \text{if } y_i = k_{t,i}, \\ I^{\text{extr}}, & \text{if } y_i = K_{t,i} \end{cases} \quad (17)$$

and \hat{I}_i is given by (15). Note that this is equivalent to the solution presented in [42].

The results for this experiment are summarized in Table 8, from which it is clear that modeling the raw GHI values yields the worst results by a large margin. This is especially true for $\mathcal{D}^{\text{folsom}}$, where there is almost a 50% improvement when using other target variables. Regarding the other target variables, the results are a little more inconclusive, since they are all within

one standard deviation of each other and different targets being only slightly better in different datasets.

5.2.4. Camera Exposure

As shown in Figure 2, the images in $\mathcal{D}^{\text{sirta}}$ and $\mathcal{D}^{\text{nrel}}$ provide two different camera exposure levels, a long exposure form and a short exposure form. Although we use the long exposure form as our default value for all other experiments, the short exposure form provides more detail in the Sun disk area at the cost of providing less detail everywhere else. We hypothesize that in the nowcasting task, predicting the irradiance value given a short exposure image is a much easier task, since the only region of interest is the area around the Sun. To test this hypothesis, we train and evaluate models using the short exposure images in $\mathcal{D}^{\text{sirta}}$ and $\mathcal{D}^{\text{nrel}}$ and compare the results to their long exposure counterparts. $\mathcal{D}^{\text{folsom}}$ was not used in this experiment since it only provides one exposure form.

From the results presented in Table 9, using short exposure images increases the performance by a significant margin under cloudy sky conditions in $\mathcal{D}^{\text{sirta}}$, while maintaining almost the same performance under clear sky conditions. Since the majority of samples in this dataset are cloudy samples (see Table 2), the performance for the entire test set is also significantly better using short exposure images. However, in $\mathcal{D}^{\text{nrel}}$, it is the clear sky performance that increases, while the cloudy sky remains the same.

5.2.5. Sample Interval

In this experiment we change the size of the training set by increasing the sample interval from 1 to 10 minutes. Since in $\mathcal{D}^{\text{nrel}}$ the minimum sample interval is 10 minutes, we do not search for any sample interval values using this dataset. All other configurations are kept at their defaults values. Our main goal with this experiment is to investigate if the larger error metrics in $\mathcal{D}^{\text{nrel}}$ are due to the higher sample interval in this dataset.

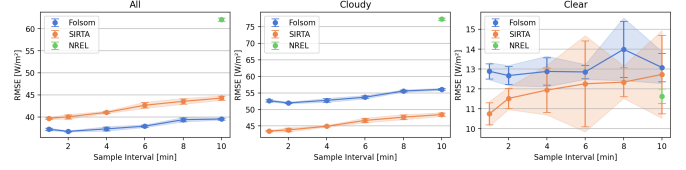


Figure 12: Test set RMSE for different sample intervals applied only to the training set. Only a single marker is shown for $\mathcal{D}^{\text{nrel}}$ since the minimum sample interval in this dataset is 10 minutes. The 1 minute sample interval value for $\mathcal{D}^{\text{sirta}}$ is only for the 2017 training year, since in 2018 the minimum sample value is 2 minutes.

The results depicted in Figure 12 show that the test RMSE steadily increases with the larger sample intervals for the “All” and “Cloudy” subsets, however at a 10 minute interval the results for both $\mathcal{D}^{\text{folsom}}$ and $\mathcal{D}^{\text{sirta}}$ are still far better than for $\mathcal{D}^{\text{nrel}}$, which indicates that the latter is a much harder dataset under cloudy sky conditions. However, for the “Clear” subset, a increasing the sample interval also deteriorates the performance, but much less so than in the other subsets. This is because clear sky conditions are very easy to model, such that little information will be gained by decreasing the sample interval. Interestingly, the test RMSE in $\mathcal{D}^{\text{nrel}}$ under clear sky conditions was very similar to the other two datasets.

5.2.6. Sun Mask

In the Sun mask experiment, we compare the model performance for 4 different combinations: 1) GHI target with no mask; 2) k_t target with no mask; 3) GHI target with mask; 4) k_t target with mask. In 3) and 4), we append the Sun mask described in subsection 3.7 as a fourth channel to the RGB input image. This implies that the first convolutional layer of the model needs to be redesigned such that it accepts a 4-channel input, which also means that the kernel weights corresponding to this additional channel need to be randomly initialized, since no pre-trained

Table 8: Test set results for all 5 different model target variables. The best performing target is highlighted in green for each dataset.

Dataset	Sky cond.	RMSE [W/m ²]			MAE [W/m ²]		
		All	Cloudy	Clear	All	Cloudy	Clear
Folsom	GHI	65.77 ± 2.22	82.62 ± 2.81	46.09 ± 1.80	48.24 ± 2.22	57.44 ± 2.29	40.14 ± 2.38
	k_t	37.11 ± 0.21	52.51 ± 0.33	12.72 ± 0.24	20.44 ± 0.19	32.66 ± 0.26	9.69 ± 0.26
	K_t	38.16 ± 0.62	53.09 ± 0.76	16.02 ± 0.90	22.09 ± 0.60	33.42 ± 0.70	12.12 ± 0.63
	k_t (weighted)	37.46 ± 0.15	52.87 ± 0.21	13.35 ± 0.45	21.02 ± 0.20	33.33 ± 0.32	10.19 ± 0.36
	K_t (weighted)	38.93 ± 0.66	53.87 ± 0.74	17.17 ± 0.89	23.06 ± 0.69	34.39 ± 0.71	13.08 ± 0.75
SIRTA	GHI	50.84 ± 2.18	54.29 ± 2.24	29.95 ± 3.10	34.69 ± 1.92	36.93 ± 1.91	24.30 ± 2.80
	k_t	39.90 ± 0.40	43.68 ± 0.45	11.35 ± 0.60	23.29 ± 0.22	26.49 ± 0.28	8.47 ± 0.50
	K_t	39.33 ± 0.43	42.91 ± 0.42	13.39 ± 1.14	23.13 ± 0.45	25.89 ± 0.35	10.33 ± 0.99
	k_t (weighted)	39.88 ± 0.31	43.72 ± 0.35	10.22 ± 0.42	23.34 ± 0.24	26.70 ± 0.31	7.78 ± 0.27
	K_t (weighted)	39.23 ± 0.28	42.94 ± 0.30	11.30 ± 0.80	22.97 ± 0.28	26.04 ± 0.26	8.71 ± 0.73
NREL	GHI	66.28 ± 0.68	82.10 ± 0.86	16.57 ± 0.19	36.05 ± 0.34	50.01 ± 0.54	11.57 ± 0.15
	k_t	62.23 ± 0.21	77.58 ± 0.26	10.46 ± 0.14	31.18 ± 0.22	44.66 ± 0.30	7.55 ± 0.14
	K_t	62.19 ± 0.32	77.44 ± 0.39	11.54 ± 0.10	31.36 ± 0.25	44.42 ± 0.37	8.46 ± 0.10
	k_t (weighted)	61.66 ± 0.10	76.87 ± 0.15	10.26 ± 0.59	31.02 ± 0.19	44.49 ± 0.12	7.40 ± 0.42
	K_t (weighted)	61.96 ± 0.32	77.18 ± 0.40	11.32 ± 0.16	31.34 ± 0.12	44.44 ± 0.13	8.36 ± 0.13

Table 9: Test set results using the two camera exposures available in $\mathcal{D}^{\text{sirta}}$ and $\mathcal{D}^{\text{nrel}}$.

Dataset	Exposure	RMSE [W/m ²]			MAE [W/m ²]		
		All	Cloudy	Clear	All	Cloudy	Clear
SIRTA	Long	39.68 ± 0.21	43.46 ± 0.22	10.75 ± 0.56	23.06 ± 0.16	26.30 ± 0.14	8.07 ± 0.42
	Short	36.46 ± 0.31	39.86 ± 0.34	11.19 ± 0.45	21.62 ± 0.15	24.58 ± 0.15	7.93 ± 0.31
NREL	Long	62.10 ± 0.37	77.31 ± 0.50	11.63 ± 0.82	31.47 ± 0.32	44.54 ± 0.34	8.54 ± 0.72
	Short	62.16 ± 0.20	77.56 ± 0.26	9.54 ± 0.22	30.43 ± 0.16	43.86 ± 0.24	6.88 ± 0.16

weights are available. All other configurations are kept at their default values presented in Table 5.

In Table 10 we show the nowcasting results for the different mask/target combinations, and compare it to [22]. Even though they used a different testing year for $\mathcal{D}^{\text{folsom}}$, we were also able to confirm, for all three datasets, that appending a Sun mask as a fourth channel to the input improves the model performance when the GHI is its target. However, when the k_t is the target, the Sun mask actually degrades the model performance. We hypothesize that this is because of the fact that the Sun position in the image is less relevant when modeling the k_t , as discussed in subsection 5.2.3, such that appending a Sun mask would mostly add redundant information to the model, which could increase the risk of over-fitting the training set. Another possible explanation is the necessary redesign of the model to accept a 4-channel input, which forced a random weight initialization in the added weights of the first layer of the model. Since all other weights are initialized with their pre-trained values, this can disrupt the pre-learned low-level features extracted by the first layer.

6. Conclusion

Due to the intermittent nature of solar PV energy, the growing integration of this energy source into the electrical grid presents several technical challenges, such as optimizing the operational cost of the grid and maintaining its frequency and voltage stability. To address this issue, recent studies have applied deep learning-based architectures and methods to forecast the

short-term irradiance (or PV power) with the use of sky-image data, due to their high spatio-temporal resolution. Although most studies focus on the forecasting problem directly, this study prioritizes the nowcasting problem, which can be coupled with video prediction models to predict the future irradiance value. We benchmark 10 different model architectures and perform several ablation experiments to show that the choice of architecture can have large impacts on the quality of the predictions, as well as the choice of the data processing pipeline, such as applying a Δt to the irradiance measurements, using a clear sky model to normalize the measurements, appending a Sun mask to the images, among others. We explored three different datasets that are commonly used by the solar forecasting community and show that our findings are consistent and can be validated across them all. In one of these datasets, we highlight a possible error related to the timestamps of the image data and provide a potential fix that we recommend readers use in future studies.

Declaration of Competing Interest

The authors declare that they have no competing interests.

Data Availability

All three datasets used in this study are publicly available online. The Folsom dataset [32] is available at <https://doi.org/10.5281/zenodo.2826939>. The NREL dataset [46] is available at <https://doi.org/10.7799/1052221>. The SIRTA dataset [39] can be requested by filling out a data request form, which is to be found at the SIRTA observatory website.

Table 10: Sun mask results for the testing set in all three datasets. Note that the approach of [22] uses 2014 in $\mathcal{D}^{\text{folsom}}$ as the testing set, but in our approach we use 2016.

Dataset	Target	RMSE [W/m ²]		MAE [W/m ²]	
		GHI	k_t	GHI	k_t
Folsom	No Mask [22]	64.83	-	37.23	-
	Mask [22]	60.31	-	36.02	-
	No Mask [Ours]	68.26 ± 3.02	37.59 ± 0.49	51.04 ± 3.13	21.00 ± 0.54
	Mask [Ours]	56.60 ± 4.95	39.90 ± 0.52	41.18 ± 5.13	22.79 ± 0.40
SIRTA	No Mask	48.67 ± 0.90	39.76 ± 0.34	33.05 ± 0.63	23.21 ± 0.17
	Mask	43.67 ± 1.51	40.83 ± 0.74	27.31 ± 1.45	24.04 ± 0.69
NREL	No Mask	66.35 ± 0.72	62.03 ± 0.33	36.28 ± 0.42	31.08 ± 0.25
	Mask	65.57 ± 0.70	64.65 ± 0.40	35.52 ± 0.29	32.32 ± 0.12

Acknowledgements

The authors would like to acknowledge the SIRTA observatory for kindly providing the sky image and irradiance data used in this study. The authors would also like to acknowledge the authors of the Folsom and NREL datasets, for open-sourcing their respective datasets.

The work of D. Silva was supported in part by the Brazilian National Council for Scientific and Technological Development (CNPq-Brazil) under Grant 304619/2022-1.

References

- [1] E. Kabir, P. Kumar, S. Kumar, A. A. Adelodun, K.-H. Kim, Solar energy: Potential and future prospects, *Renewable and Sustainable Energy Reviews* 82 (2018) 894–900. doi:10.1016/j.rser.2017.09.094.
- [2] E. Liu, J. Bebic, Distribution System Voltage Performance Analysis for High-Penetration Photovoltaics, Tech. Rep. NREL/SR-581-42298, 924648 (Feb. 2008). doi:10.2172/924648.
- [3] N. Kakimoto, Q.-Y. Piao, H. Ito, Voltage Control of Photovoltaic Generator in Combination With Series Reactor, *IEEE Transactions on Sustainable Energy* 2 (4) (2011) 374–382. doi:10.1109/TSTE.2011.2148181.
- [4] S. Eftekharijad, G. T. Heydt, V. Vittal, Optimal Generation Dispatch With High Penetration of Photovoltaic Generation, *IEEE Transactions on Sustainable Energy* 6 (3) (2015) 1013–1020. doi:10.1109/TSTE.2014.2327122.
- [5] M. Fan, V. Vittal, G. T. Heydt, R. Ayyanar, Probabilistic Power Flow Analysis With Generation Dispatch Including Photovoltaic Resources, *IEEE Transactions on Power Systems* 28 (2) (2013) 1797–1805. doi:10.1109/TPWRS.2012.2219886.
- [6] L. Bird, M. Milligan, D. Lew, Integrating Variable Renewable Energy: Challenges and Solutions, Tech. Rep. NREL/TP-6A20-60451, 1097911 (Sep. 2013). doi:10.2172/1097911.
- [7] R. Shah, N. Mithulananthan, R. Bansal, V. Ramachandaramurthy, A review of key power system stability challenges for large-scale PV integration, *Renewable and Sustainable Energy Reviews* 41 (2015) 1423–1436. doi:10.1016/j.rser.2014.09.027.
- [8] R. A. Rajagukguk, R. A. A. Ramadhan, H.-J. Lee, A Review on Deep Learning Models for Forecasting Time Series Data of Solar Irradiance and Photovoltaic Power, *Energies* 13 (24) (2020) 6623. doi:10.3390/en13246623.
- [9] H. Wen, Y. Du, X. Chen, E. Lim, H. Wen, L. Jiang, W. Xiang, Deep Learning Based Multistep Solar Forecasting for PV Ramp-Rate Control Using Sky Images, *IEEE Transactions on Industrial Informatics* 17 (2) (2021) 1397–1406. doi:10.1109/TII.2020.2987916.
- [10] K. He, X. Zhang, S. Ren, J. Sun, Deep Residual Learning for Image Recognition (Dec. 2015). arXiv:1512.03385.
- [11] H. Yang, L. Wang, C. Huang, X. Luo, 3D-CNN-Based Sky Image Feature Extraction for Short-Term Global Horizontal Irradiance Forecasting, *Water* 13 (13) (2021) 1773. doi:10.3390/w13131773.
- [12] D. Tran, L. Bourdev, R. Fergus, L. Torresani, M. Paluri, Learning Spatiotemporal Features with 3D Convolutional Networks (Oct. 2015). arXiv:1412.0767.
- [13] Q. Paletta, G. Arbod, J. Lasenby, Benchmarking of deep learning irradiance forecasting models from sky images – An in-depth analysis, *Solar Energy* 224 (2021) 855–867. doi:10.1016/j.solener.2021.05.056.
- [14] J. Liu, H. Zang, L. Cheng, T. Ding, Z. Wei, G. Sun, A Transformer-based multimodal-learning framework using sky images for ultra-short-term solar irradiance forecasting, *Applied Energy* 342 (2023) 121160. doi:10.1016/j.apenergy.2023.121160.
- [15] A. Vaswani, N. Shazeer, N. Parmar, J. Uszkoreit, L. Jones, A. N. Gomez, L. Kaiser, I. Polosukhin, Attention Is All You Need (Aug. 2023). arXiv:1706.03762.
- [16] A. Dosovitskiy, L. Beyer, A. Kolesnikov, D. Weissenborn, X. Zhai, T. Unterthiner, M. Dehghani, M. Minderer, G. Heigold, S. Gelly, J. Uszkoreit, N. Houlsby, An Image is Worth 16x16 Words: Transformers for Image Recognition at Scale (Jun. 2021). arXiv:2010.11929.
- [17] C. Feng, J. Zhang, SolarNet: A sky image-based deep convolutional neural network for intra-hour solar forecasting, *Solar Energy* 204 (2020) 71–78. doi:10.1016/j.solener.2020.03.083.
- [18] K. Simonyan, A. Zisserman, Very Deep Convolutional Networks for Large-Scale Image Recognition (Apr. 2015). arXiv:1409.1556.
- [19] Y. Sun, V. Venugopal, A. R. Brandt, Short-term solar power forecast with deep learning: Exploring optimal input and output configuration, *Solar Energy* 188 (2019) 730–741. doi:10.1016/j.solener.2019.06.041.
- [20] Y. Nie, E. Zelikman, A. Scott, Q. Paletta, A. Brandt, SkyGPT: Probabilistic ultra-short-term solar forecasting using synthetic sky images from physics-constrained VideoGPT, *Advances in Applied Energy* 14 (2024) 100172. doi:10.1016/j.adapen.2024.100172.
- [21] O. Ronneberger, P. Fischer, T. Brox, U-Net: Convolutional Networks for Biomedical Image Segmentation (May 2015). arXiv:1505.04597.
- [22] E. A. Papatheofanous, V. Kalekis, G. Venitourakis, F. Tziolos, D. Reisis, Deep Learning-Based Image Regression for Short-Term Solar Irradiance Forecasting on the Edge, *Electronics* 11 (22) (2022) 3794. doi:10.3390/electronics11223794.
- [23] Y. Nie, X. Li, A. Scott, Y. Sun, V. Venugopal, A. Brandt, SKIPP'D: A SKY Images and Photovoltaic Power Generation Dataset for short-term solar forecasting, *Solar Energy* 255 (2023) 171–179. doi:10.1016/j.solener.2023.03.043.
- [24] Glossary of solar radiation resource terms: National Renewable Energy Laboratory.
- [25] F. Antonanzas-Torres, R. Urraca, J. Polo, O. Perpiñán-Lamigueiro, R. Escobar, Clear sky solar irradiance models: A review of seventy models, *Renewable and Sustainable Energy Reviews* 107 (2019) 374–387. doi:10.1016/j.rser.2019.02.032.
- [26] X. Sun, J. M. Bright, C. A. Gueymard, B. Acord, P. Wang, N. A. Engerer, Worldwide performance assessment of 75 global clear-sky irradiance models using Principal Component Analysis, *Renewable and Sustainable Energy Reviews* 111 (2019) 550–570. doi:10.1016/j.rser.2019.04.006.
- [27] P. Ineichen, A broadband simplified version of the Solis clear sky model, *Solar Energy* 82 (8) (2008) 758–762. doi:10.1016/j.solener.2008.02.009.
- [28] L. R. Do Nascimento, T. De Souza Viana, R. A. Campos, R. Rütger, Extreme solar overirradiance events: Occurrence and impacts on utility-scale photovoltaic power plants in Brazil, *Solar Energy* 186 (2019) 370–381. doi:10.1016/j.solener.2019.05.008.
- [29] R. H. Inman, H. T. Pedro, C. F. Coimbra, Solar forecasting methods for renewable energy integration, *Progress in Energy and Combustion Science* 39 (6) (2013) 535–576. doi:10.1016/j.pecs.2013.06.002.
- [30] C. A. Gueymard, J. M. Bright, D. Lingfors, A. Habte, M. Sengupta, A posteriori clear-sky identification methods in solar irradiance time series: Review and preliminary validation using sky imagers, *Renewable and Sustainable Energy Reviews* 109 (2019) 412–427. doi:10.1016/j.rser.2019.04.027.
- [31] M. J. Reno, C. W. Hansen, Identification of periods of clear sky irradiance in time series of GHI measurements, *Renewable Energy* 90 (2016) 520–531. doi:10.1016/j.renene.2015.12.031.
- [32] H. T. C. Pedro, D. P. Larson, C. F. M. Coimbra, A comprehensive dataset for the accelerated development and benchmarking of solar forecasting methods, *Journal of Renewable and Sustainable Energy* 11 (3) (2019) 036102. doi:10.1063/1.5094494.
- [33] D. Yang, D. Van Der Meer, J. Munkhammar, Probabilistic solar forecasting benchmarks on a standardized dataset at Folsom, California, *Solar Energy* 206 (2020) 628–639. doi:10.1016/j.solener.2020.05.020.
- [34] K. Song, K. Wang, S. Wang, N. Wang, J. Zhang, K. Zhang, H. Wei, Intra-hour solar irradiance forecasting: An end-to-end Transformer-based network, in: 2024 39th Youth Academic Annual Conference of Chinese Association of Automation (YAC), IEEE, Dalian, China, 2024, pp. 544–549. doi:10.1109/YAC63405.2024.10598711.
- [35] Z. Wang, L. Wang, C. Huang, X. Luo, A Hybrid Ensemble Learning Model for Short-Term Solar Irradiance Forecasting Using Historical Observations and Sky Images, *IEEE Transactions on Industry Applications* 59 (2) (2023) 2041–2049. doi:10.1109/TIA.2022.3231842.
- [36] G. Ruan, X. Chen, E. G. Lim, L. Fang, Q. Su, L. Jiang, Y. Du, On the use of sky images for intra-hour solar forecasting benchmarking: Comparison of indirect and direct approaches, *Solar Energy* 276 (2024) 112649. doi:10.1016/j.solener.2024.112649.

- [37] L. Zhang, R. Wilson, M. Sumner, Y. Wu, Advanced multimodal fusion method for very short-term solar irradiance forecasting using sky images and meteorological data: A gate and transformer mechanism approach, *Renewable Energy* 216 (2023) 118952. doi:10.1016/j.renene.2023.118952.
- [38] J. Nunes Maciel, J. Javier Gimenez Ledesma, O. Hideo Ando Junior, Hybrid prediction method of solar irradiance applied to short-term photovoltaic energy generation, *Renewable and Sustainable Energy Reviews* 192 (2024) 114185. doi:10.1016/j.rser.2023.114185.
- [39] M. Haeffelin, L. Barthès, O. Bock, C. Boitel, S. Bony, D. Bouniol, H. Cheffer, M. Chiriaco, J. Cuesta, J. Delanoë, P. Drobinski, J.-L. Dufresne, C. Flamant, M. Grall, A. Hodzic, F. Hourdin, F. Lapouge, Y. Lemaître, A. Mathieu, Y. Morille, C. Naud, V. Noël, W. O'Hirok, J. Pelon, C. Pietras, A. Protat, B. Romand, G. Scialom, R. Vautard, SARTA, a ground-based atmospheric observatory for cloud and aerosol research, *Annales Geophysicae* 23 (2) (2005) 253–275. doi:10.5194/angeo-23-253-2005.
- [40] Q. Paletta, A. Hu, G. Arbod, J. Lasenby, ECLIPSE: Envisioning CLOUD Induced Perturbations in Solar Energy, *Applied Energy* 326 (2022) 119924. doi:10.1016/j.apenergy.2022.119924.
- [41] M. Jain, P. Yadav, S. Dev, Holistic and Lightweight Approach for Solar Irradiance Forecasting, *IEEE Transactions on Geoscience and Remote Sensing* (2024) 1–1. doi:10.1109/tgrs.2024.3415413.
- [42] Q. Paletta, Y. Nie, Y.-M. Saint-Drenan, B. Le Saux, Improving cross-site generalisability of vision-based solar forecasting models with physics-informed transfer learning, *Energy Conversion and Management* 309 (2024) 118398. doi:10.1016/j.enconman.2024.118398.
- [43] Y. Nie, Q. Paletta, A. Scott, L. M. Pomares, G. Arbod, S. Sgouridis, J. Lasenby, A. Brandt, Sky image-based solar forecasting using deep learning with heterogeneous multi-location data: Dataset fusion versus transfer learning, *Applied Energy* 369 (2024) 123467. doi:10.1016/j.apenergy.2024.123467.
- [44] I. M. Insaf, H. M. K. D. Wickramathilaka, M. A. N. Upendra, G. M. R. I. Godaliyadda, M. P. B. Ekanayake, H. M. V. R. Herath, D. M. L. H. Dissawa, J. B. Ekanayake, Global Horizontal Irradiance Modeling from Sky Images Using ResNet Architectures, in: 2021 IEEE 16th International Conference on Industrial and Information Systems (ICIS), IEEE, Kandy, Sri Lanka, 2021, pp. 239–244. doi:10.1109/ICIIIS53135.2021.9660664.
- [45] L. Al Asmar, L. Musson-Genon, E. Dupont, J.-C. Dupont, K. Sartelet, Improvement of solar irradiance modelling during cloudy-sky days using measurements, *Solar Energy* 230 (2021) 1175–1188. doi:10.1016/j.solener.2021.10.084.
- [46] T. Stoffel, A. Andreas, NREL Solar Radiation Research Laboratory (SRRL): Baseline Measurement System (BMS); Golden, Colorado (Data) (1981). doi:10.7799/1052221.
- [47] A. L. Jonathan, D. Cai, C. C. Ukwuoma, N. J. J. Nkou, Q. Huang, O. Bamisile, A radiant shift: Attention-embedded CNNs for accurate solar irradiance forecasting and prediction from sky images, *Renewable Energy* 234 (2024) 121133. doi:10.1016/j.renene.2024.121133.
- [48] H. Gao, M. Liu, Short-term Solar Irradiance Prediction from Sky Images with a Clear Sky Model, in: 2022 IEEE/CVF Winter Conference on Applications of Computer Vision (WACV), IEEE, Waikoloa, HI, USA, 2022, pp. 3074–3082. doi:10.1109/WACV51458.2022.00313.
- [49] H.-M. Zuo, J. Qiu, Y.-H. Jia, Q. Wang, F.-F. Li, Ten-minute prediction of solar irradiance based on cloud detection and a long short-term memory (LSTM) model, *Energy Reports* 8 (2022) 5146–5157. doi:10.1016/j.egy.2022.03.182.
- [50] C. Feng, J. Zhang, W. Zhang, B.-M. Hodge, Convolutional neural networks for intra-hour solar forecasting based on sky image sequences, *Applied Energy* 310 (2022) 118438. doi:10.1016/j.apenergy.2021.118438.
- [51] G. Parmar, R. Zhang, J.-Y. Zhu, On Aliased Resizing and Surprising Subtleties in GAN Evaluation (Jan. 2022). arXiv:2104.11222.
- [52] F. Bettonvil, Fisheye lenses, WGN, *Journal of the International Meteorological Organization* 33 (2005) 9–14.
- [53] P. Izmailov, D. Podoprikin, T. Garipov, D. Vetrov, A. G. Wilson, Averaging Weights Leads to Wider Optima and Better Generalization (Feb. 2019). arXiv:1803.05407.
- [54] M. Tan, Q. V. Le, EfficientNetV2: Smaller Models and Faster Training (Jun. 2021). arXiv:2104.00298.
- [55] I. Radosavovic, R. P. Kosaraju, R. Girshick, K. He, P. Dollár, Designing Network Design Spaces (Mar. 2020). arXiv:2003.13678.
- [56] M. Sandler, A. Howard, M. Zhu, A. Zhmoginov, L.-C. Chen, MobileNetV2: Inverted Residuals and Linear Bottlenecks (Mar. 2019). arXiv:1801.04381.
- [57] P. I. Frazier, A Tutorial on Bayesian Optimization (Jul. 2018). arXiv:1807.02811.
- [58] D. P. Kingma, J. Ba, Adam: A Method for Stochastic Optimization (Jan. 2017). arXiv:1412.6980.
- [59] I. Loshchilov, F. Hutter, Decoupled Weight Decay Regularization (Jan. 2019). arXiv:1711.05101.
- [60] J. Zhang, A. Florita, B.-M. Hodge, S. Lu, H. F. Hamann, V. Banunaryanan, A. M. Brockway, A suite of metrics for assessing the performance of solar power forecasting, *Solar Energy* 111 (2015) 157–175. doi:10.1016/j.solener.2014.10.016.
- [61] L. Frías-Paredes, F. Mallor, T. León, M. Gastón-Romeo, Introducing the Temporal Distortion Index to perform a bidimensional analysis of renewable energy forecast, *Energy* 94 (2016) 180–194. doi:10.1016/j.energy.2015.10.093.
- [62] L. Vallance, B. Charbonnier, N. Paul, S. Dubost, P. Blanc, Towards a standardized procedure to assess solar forecast accuracy: A new ramp and time alignment metric, *Solar Energy* 150 (2017) 408–422. doi:10.1016/j.solener.2017.04.064.